



Published in final edited form as:

Nat Methods. 2008 August ; 5(8): 695–702. doi:10.1038/nmeth.1237.

Robust single particle tracking in live cell time-lapse sequences

Khuloud Jaqaman^{1,*}, Dinah Loerke¹, Marcel Mettlen¹, Hirotaka Kuwata², Sergio Grinstein², Sandra L. Schmid¹, and Gaudenz Danuser¹

¹Department of Cell Biology, The Scripps Research Institute, 10550 N. Torrey Pines Rd, La Jolla, CA, USA, 92037

²Department of Cell Biology, The Hospital for Sick Children, 555 University Ave, Toronto, ON, Canada, M5G1X8

Abstract

Single particle tracking (SPT) is often the rate-limiting step in live cell imaging studies of sub-cellular dynamics. Here we present a tracking algorithm that addresses the principal challenges of SPT, namely high particle density, particle motion heterogeneity, temporary particle disappearance, and particle merging and splitting. The algorithm first links particles between consecutive frames and then links the resulting track segments into complete trajectories. Both steps are formulated as global combinatorial optimization problems whose solution identifies the overall most likely set of particle trajectories throughout the movie. Using this approach, we show that the GTPase dynamin differentially affects the kinetics of long and short-lived endocytic structures, and that the motion of CD36 receptors along cytoskeleton-mediated linear tracks increases their aggregation probability. Both applications indicate the requirement for robust and complete tracking of dense particle fields to dissect the mechanisms of receptor organization at the level of the plasma membrane.

With the development of bright fluorescent probes, stable microscopes and sensitive cameras, live cell imaging has become a standard technique to study sub-cellular dynamics. The resulting images often consist of punctate features, representing small molecular assemblies or even single molecules^{1–3}. To gain insight into the molecular mechanisms that drive the observed dynamics, such experiments must be combined with single particle tracking (SPT) that captures the full spatio-temporal complexity of sub-cellular particle behavior.

SPT faces several challenges that in practice hinder such studies. Importantly, SPT goes beyond the detection and localization of particles; its key step is the establishment of correspondence between particle images in a sequence of frames. Establishing

Users may view, print, copy, and download text and data-mine the content in such documents, for the purposes of academic research, subject always to the full Conditions of use:http://www.nature.com/authors/editorial_policies/license.html#terms

*kjaqaman@scripps.edu.

Author contributions

KJ designed and implemented the tracking algorithm and performed the analysis of CD36 aggregation. She wrote the majority of the manuscript. DL performed the analysis of CCP lifetimes and contributed the related sections to the manuscript. MM and HK acquired live cell image sequences of EGFP-clathrin light chain and Cy3 Fab-fragment labeled CD36 receptors, respectively. SG, SS, and GD initiated the study and helped with editing of the manuscript.

correspondence is complicated by various factors, most notably high particle density, particle motion heterogeneity, temporary particle disappearance (e.g. due to out-of-focus motion and detection failure), particle merging (i.e. two particles approaching each other within distances below the resolution limit), and particle splitting (i.e. two unresolved particles diverging to resolvable distances)^{4, 5}. Historically, many of these challenges have been overcome by diluting the fluorescent probes, resulting in a low particle density with almost unambiguous particle correspondence^{6, 7}. Under such conditions, particle tracking is indeed reduced to a simple particle detection and localization problem⁸. However, while low particle densities reveal motion characteristics^{1–3, 9, 10}, they do not allow probing of the interactions between particles¹¹. Also, the amount of data collected per experiment is low, limiting the observation of spatially and temporally heterogeneous particle behavior and hindering the capture of infrequent events. Furthermore, even with low particle density, low signal-to-noise ratio (SNR) and probe flicker complicate the search for particle correspondence. Therefore, for most cell biological studies, there is a great need for robust SPT methods that address the challenges mentioned above.

The most accurate solution to SPT is provided by the method of multiple-hypothesis tracking (MHT)¹². In MHT, given particle positions in every frame, all particle paths within the bounds of expected particle behavior are constructed throughout the whole movie. The largest non-conflicting ensemble of paths is then chosen as the solution, where non-conflicting means that no two paths share in any frame the image of the same particle. This solution is globally optimal in both space and time, i.e. it is the best solution that can be found by simultaneously accounting for all particle positions at all time points. Clearly, MHT is computationally prohibitive even for problems with a few tens of particles tracked over a few tens of frames. Therefore, heuristic algorithms with higher computational efficiency have been proposed to approximate the MHT solution. Most of these algorithms are *greedy*, i.e. they seek to approach the globally optimal solution by taking a series of locally optimal solutions. Usually, this means that particle correspondence is determined step-by-step between consecutive frames¹³, reducing computational complexity at the expense of temporal globality. Many tracking algorithms then solve the frame-to-frame correspondence problem in a spatially global manner^{14–20}, and seek to recover tracks after temporary particle disappearance^{14–18, 21}. Some algorithms treat merging and splitting as a temporary disappearance of one of the particles^{14–16}, while others treat them as separate events^{20, 22}. Racine et al.²³ are unique in their approach to SPT in that they use kymograms to maximally benefit from temporal information and thus avoid many of the problems of greedy algorithms. However, their method cannot track Brownian motion and is thus not generally applicable. While the many existing algorithms address one or the other of the issues in SPT, none of them tackles all the issues simultaneously. Consequently, investigators must sacrifice some tracking aspects for the sake of others, based on their specific application.

Here we present a tracking algorithm that uses one mathematical framework, the linear assignment problem (LAP)^{24, 25}, to provide an accurate solution to all the SPT challenges listed above. Given a set of detected particles throughout a time-lapse image sequence, the algorithm first links the detected particles between consecutive frames, and then links the

track segments generated in the first step to simultaneously close gaps and capture particle merge and split events. Thus, while the initial particle assignment is temporally greedy, the subsequent track assignment is accomplished via temporally global optimization, overcoming the shortcomings of algorithms relying solely on greedy assignment strategies. Both steps employ global optimization in space. Overall, this approach defines an accurate, yet computationally feasible, approximation to MHT, allowing the robust tracking of particles under high density conditions.

We demonstrate our approach based on two applications that critically depend on tracking robustness and globality: (1) Accurate, comprehensive lifetime analysis of endocytic clathrin-coated pits (CCPs), and (2) single molecule tracking of the macrophage trans-membrane receptor CD36, revealing receptor aggregation and dissociation events.

Results

Tracking via spatially and temporally global assignments

Given the set of detected particles in a live cell time-lapse sequence (Supplementary Notes 1, 2 online present the detection algorithms used for the two applications shown in this work and their performance), we generated particle tracks in two steps (Fig. 1a): First, we constructed track segments by linking the detected particles between consecutive frames, under the condition that a particle in one frame could link to at most one particle in the previous or following frame. These track segments started and ended not only due to the true appearance and disappearance of particles, but also due to apparent disappearances associated with limitations in imaging and SNR, for example when a particle temporarily moved out of the plane in focus, or when two particles approached each other within a distance smaller than the resolution limit. The track segments obtained in this step tended to be incomplete, resulting in a systematic underestimation of particle lifetimes. In addition, because of the one-to-one assignment of particles, this step could not capture particle merges and splits, which by definition required one particle in one frame to be assigned to two particles in the previous or subsequent frame, respectively. Therefore, in a second step, we linked the initial track segments in three ways: End-to-start, in order to close gaps resulting from temporary disappearance, end-to-middle, in order to capture merging events, and start-to-middle, in order to capture splitting events.

We formulated both the frame-to-frame particle linking step and the gap closing, merging and splitting step as LAPs^{24, 25}. In the LAP framework, every potential assignment (particle assignment in the first step, track segment assignment in the second step) was characterized by a cost (matrix entries $C_{ij} = \ell_{ij}, x, b, d$ in Fig. 1b and $C_{ij} = g_{ij}, m_{ij}, s_{ij}, x, b, b', d, d'$ in Fig. 1c). The goal of solving the LAP in each step was then to identify the combination of assignments with the minimal sum of costs:

$$\hat{A} = \underset{\text{arg min}}{\sum_{i=1}^{\text{number of rows}} \sum_{j=1}^{\text{number of columns}} A_{ij} C_{ij}}, \quad (1)$$

such that

$$\sum_{i=1}^{\text{number of rows}} A_{ij}=1 \& \sum_{j=1}^{\text{number of columns}} A_{ij}=1. \quad (2)$$

In Eq. 1, A is any assignment matrix with entries = 1 (link) and 0 (no link), and \hat{A} is the assignment matrix with minimal sum of costs. The conditions on A (and consequently \hat{A}) in Eq. 2 guaranteed that the selected assignments were mutually exclusive, i.e. no particle or track segment could be included in more than one assignment. Thus, when a particle or track segment had multiple potential assignments, the assignments competed with one another. While assignments with a lower cost tended to win, the requirement for a globally minimized cost could result in the selection of assignments where the costs were not the lowest.

In the frame-to-frame particle linking step, three types of potential assignments were in competition (Fig. 1b). A particle in the source frame t could link to a particle in the target frame $t + 1$ (cost function ℓ). Alternatively, a particle in the source frame could link to nothing, leading to a track segment end (cost function d), or a particle in the target frame could get linked by nothing, leading to a track segment start (cost function b). The decision between these possibilities was made globally in space (Eqs. 1, 2). However, the assignment was temporally greedy since it was based on particle configuration in the specific source and target frames only.

In the gap closing, merging and splitting step, six types of potential assignments were in competition (Fig. 1c). The end of a track segment could link to the start of another track segment, thus closing a gap (cost function g), the end of a track segment could link to a middle point of another track segment, leading to a merge (cost function m), or the start of a track segment could get linked by a middle point of another track segment, leading to a split (cost function s). Alternatively, the end of a track segment could link to nothing, leading to a track termination (cost function d), the start of a track segment could get linked by nothing, leading to a track initiation (cost function b) or the track segment middle points introduced for merging and splitting could link to nothing, refusing a merge or a split (cost functions d' and b'). In this step, all track segments throughout the whole movie competed with each other. Thus, the LAP solution (Eqs. 1, 2) was global in both space and time.

The framework described up to this point is general. Its goal is to provide a robust yet computationally feasible approximation to MHT. It is independent of the actual cost functions used to weigh the various competing assignments. Thus, it is independent of problem dimensionality (we solve 2D and 3D tracking problems with the same framework; data not shown) as well as of the type of particle motion (Brownian motion, directed motion, etc.). It is also independent of the physical nature of the particle (single molecule, molecular assembly, organelle, etc.), which mainly influences the choice of an appropriate particle detection method.

The cost functions, on the other hand, must be tailored to the specific tracking application. In our implementation, this is technically solved by treating the cost functions themselves as

input variables together with their parameters. Here we demonstrate the definition of cost functions for tracking isotropic random motion, such as pure or confined Brownian motion, due to its prevalence in cell biological applications. In this case, the costs were functions of distance and intensity:

$$\ell_{ij} = \delta_{ij}^2, \quad (3)$$

$$g_{IJ} = \delta_{IJ}^2, \quad (4)$$

$$m_{IJ}, s_{IJ} = \begin{cases} \delta_{IJ}^2 \times \rho_{IJ}, & \rho_{IJ} > 1 \\ \delta_{IJ}^2 \times \rho_{IJ}^{-2}, & \rho_{IJ} < 1 \end{cases}. \quad (5)$$

In Eq. 3, δ_{ij} is the distance between particles i and j . In Eq. 4, δ_{IJ} is the distance between the end of track segment I and the start of track segment J . In Eq. 5, δ_{IJ} is the distance between the end or start of track segment I and the middle point of track segment J , while ρ_{IJ} is the ratio of the intensities A_I (of track segment I) and A_J (of track segment J) before and after merging or splitting:

$$\rho_{IJ}(\text{merge at time } t) = \frac{A_J(t)}{A_I(t-1) + A_J(t-1)}, \quad \rho_{IJ}(\text{split at time } t) = \frac{A_I(t-1)}{A_I(t) + A_J(t)}. \quad (6)$$

The intensity factor increased the cost when the intensity after merging or before splitting was different from the sum of intensities before merging or after splitting, with a higher penalty when it was smaller. This intensity penalty ensured that merging and splitting events were not picked up only due to the proximity of particle tracks, but that the associated intensity changes were consistent with the image superposition of merging or splitting particles. The alternative costs used to reject particle linking, gap closing, merging and splitting (b, b', d, d' in Fig. 1b,c) are described in Supplementary Note 3 online.

In order to exclude physically nonsensical solutions, in practice we did not allow every particle or track segment to potentially link to every particle or track segment, but rather introduced cutoffs that excluded impossible links *a priori* (x in Fig. 1b,c). For frame-to-frame particle linking and for gap closing, the cutoff was based on distance. For merging and splitting, it was based on both distance and intensity. Distance-based cutoffs were data-driven: they were derived for every particle from its observed motion, allowing for self-adaptation (Supplementary Note 3 online).

Validation of tracking algorithm on simulated tracks

We validated our algorithm by tracking simulated particles at different densities and with different signal stability. The particle density and signal stability used in the simulations were varied from conditions similar to the experimental data (Supplementary Note 5 online) to much harsher conditions, the purpose of which was to identify the breakdown of the method. Simulated particles moved in a Brownian fashion ($D = 0.75$ pixels²/frame corresponding to an average displacement between frames of 1.7 pixels, similar to the average displacement observed for CD36 receptors and CCPs), underwent merge and split

events, and their lifetimes followed a Rayleigh distribution (chosen to reflect the maturation process of molecular aggregates such as CCPs). We varied their density by gradually decreasing the average nearest neighbor distance from 12 pixels to 4 pixels, corresponding to 6% – 42% of particles having nearest neighbors that were closer than twice their average displacement between frames (Simulations 1–5, Fig. 2a). Under these conditions, particles and track segments had on average more than one potential assignment in their respective linking steps, with the number of potential assignments increasing with particle density (Fig. 2a). The tracking of particles under these high density conditions requires a global optimization approach that can resolve assignment ambiguities and conflicts.

To test the performance of the tracking algorithm independently of the detection algorithm, we simulated trajectories (ground truth; GT) and directly derived from them a list of particle positions and intensities per frame. The effect of signal stability on detection was accounted for by deleting a fraction of the particles from the list, where a lower signal stability (e.g. because of lower SNR) led to a larger fraction being deleted (Supplementary Notes 1, 2 online show the relationship between SNR and the fraction of particles missed by the detection algorithms employed). For the validation process, the fraction of particles missed by the detection algorithm was varied from 0% to 50%. We did not include false detection positives in the validation process because in practice false positives tended to have very short trajectories (2–3 frames long) which could be identified and removed from the ensemble of trajectories a posteriori.

We evaluated the tracking results in terms of the fraction of true positive and false positive links, closed gaps and merging and splitting events, relative to the GT (Fig. 2b–d). As expected, the tracking algorithm performed best for the lowest density simulation with 0% detection misses, and its performance decreased almost monotonically with increasing particle density and increasing detection misses. Under all tested conditions, there were more correct links, gaps, merges and splits than wrong ones. Importantly, even at the highest density (Simulation 5, 0% misses), where ~40% of particles had nearest neighbors closer than twice their average displacement, there were only 10% false links, demonstrating the power of a global tracking approach.

We also evaluated the tracking results in terms of the particle lifetime distribution, which we compared to the GT lifetime distribution via the Kolmogorov-Smirnov test (Fig. 2e; Supplementary Note 6 online). Lifetime measurements rely on all aspects of tracking, and thus are the most sensitive to tracking errors. Any mistakes in the particle linking or gap closing steps break up particle trajectories, resulting in the systematic underestimation of particle lifetimes. Therefore, the comparison of simulated and retrieved particle lifetime distributions was the most comprehensive performance measure for tracking. This comparison indicated that robust tracking required a trade-off between particle density and signal stability. As the particle density increased, less detection misses could be tolerated (i.e. higher signal stability was required): At the lowest density, tracking was reliable even with 50% detection misses; with no detection misses, tracking was reliable up to the highest density.

Clathrin-coated pit lifetime is regulated by dynamin

We employed our tracker to assay the lifetime of endocytic clathrin-coated pits (CCPs) in BSC1 cells expressing a fully functional clathrin light chain EGFP construct²⁶ (Fig. 3a). CCP dynamics can be visualized at high time resolution by total internal reflection fluorescence microscopy (TIR-FM)²⁷. However, it has remained a challenge to extract reliable lifetime data from TIR-FM movies, since lifetime measurements are notoriously susceptible to tracking errors, as caused for example by the temporary loss of the fluorescent signal of a CCP or by ambiguity in the assignment of CCP images between consecutive frames. As a result, tracking has previously been accomplished either manually for a low number of well-discernable CCPs^{27, 28} or using semi-automated tracking restricted to isolated and bright CCPs that do not have close neighbors that can potentially confuse the tracking algorithm^{26, 29}.

We detected CCPs using a method based on the *à trous* wavelet decomposition³⁰ (Supplementary Note 1 online). Because of the globality and gap closing feature of our tracker, we could extract complete CCP tracks independent of their brightness and position relative to other CCPs (Fig. 3b, Supplementary Video 1 online). We verified that our gap closing maximized the retrieval of tracks interrupted by temporary particle disappearance while minimizing the erroneous linking of true track terminations to true track initiations by analyzing the distribution of gap lengths identified by our tracker (Supplementary Note 7 online). First, longer gaps were less abundant than shorter gaps, indicating that the time window of eight frames chosen for gap closing captured most gaps in the system, preventing the systematic underestimation of CCP lifetimes. Second, the distribution of gap lengths, expressed in frames, was independent of frame rate (0.5 Hz vs. 2.5 Hz), demonstrating that the gaps closed resulted from detection failure in the noisy images. In contrast, the erroneous linking of true track terminations to true track initiations would have led to a gap length distribution that exhibited a characteristic time scale expressed in seconds, resulting in systematic differences between the gap length distributions expressed in frames.

We measured CCP lifetimes in control cells and in cells in which the function of dynamin, a key component of the endocytic machinery³¹, was altered (Fig. 3c,d). Overexpression of wildtype dynamin decreased the mean CCP lifetime, while dynamin knockdown with siRNA increased the mean lifetime. Treatment of cells with dynasore, a small-molecule inhibitor of dynamin³², also increased the average lifetime. Interestingly, the third quartiles of the lifetime distributions changed more dramatically than the second quartiles, suggesting that dynamin might differentially affect short and longer-lived CCP subpopulations. We explored these behaviors in more detail elsewhere (Loerke, Mettlen et al., manuscript submitted). Importantly, the differentiation between these lifetime histograms critically depended on the application of temporally global gap closing. For example, while proper gap closing revealed that the treatment of cells with dynasore increased CCP lifetimes, tracking without gap closing resulted in an apparent decrease in CCP lifetimes (Fig. 3e,f), due to the decreased stability of CCP signals under dynasore treatment. Thus, tracking without gap closing resulted in lifetime distributions that were simply a reflection of the breakage of tracks due to limited SNR, masking away the effects of dynamin on CCP maturation kinetics.

CD36 receptor aggregation activity depends on motion type

We also employed our tracker to follow the motion of the macrophage trans-membrane receptor CD36 and to characterize the aggregation state of individual surface bound CD36 molecules. At rest, CD36 is thought to exist as quiescent monomers, which are activated and internalized in response to oligomerization by multivalent ligands like oxidized LDL and malaria-infected red blood cells³³. However, we found that CD36 resided predominantly in multi-molecular complexes containing several copies of the receptor (intensity analysis of single molecule movies of CD36; Jaqaman, Kuwata et al., manuscript in preparation). The ability of our tracker to capture merging and splitting events enabled us to determine whether the observed CD36 aggregates were stable or instead underwent dissociation and re-association.

We immuno-labeled surface-bound CD36 receptors in primary macrophages by a primary Fab fragment and a Cy3-conjugated secondary Fab fragment, and recorded single-molecule movies using epi-fluorescence microscopy at a frame rate of 10 Hz (Fig. 4a, Supplementary Video 2 online). Both individual receptors and receptor aggregates generated diffraction-limited image features, i.e. particles. Thus, we estimated their positions by first detecting local maxima, and then fitting Gaussian kernels in areas around these local maxima to achieve sub-pixel localization³⁴. To enhance detection efficiency under the low SNR conditions of single molecule movies, we performed the search for local maxima in time-averaged images, followed by Gaussian kernel fitting in individual frames (Supplementary Note 2, Supplementary Video 2 online).

A substantial subset of surface-bound CD36 receptors and receptor aggregates moved along linear tracks that were radiated from the perinuclear region (Fig. 4b, Supplementary Video 3, Supplementary Note 8 online). The molecules moving along linear tracks took larger steps (both forward and backward) along the preferred direction of motion than perpendicular to it. To accurately track both subsets of CD36 molecules – those moving randomly and those moving along linear tracks – we modified the cost functions of Eqs 3–6 such that particles with significant evidence for motion along linear tracks could benefit from an explicit linear motion model (Supplementary Note 9 online describes the modified cost functions and illustrates the shortcomings of tracking CD36 molecules with the random motion model of Eqs 3–6; Supplementary Note 7 online shows detailed statistics on the recovered gaps, merges and splits in CD36 tracks).

Due to the radial arrangement of the linear CD36 tracks, we suspected that the linear component of CD36 motion was dependent on actomyosin driven flow of the cortical network and/or on microtubule-guided motors or diffusion. To test this hypothesis, we treated macrophages with either Blebbistatin to inhibit myosin II activity, or Nocodazole to depolymerize microtubules. Blebbistatin (10 μM for 10 min) stopped the linear motion almost completely (Fig. 4c, Supplementary Video 4 online). Nocodazole (50 μM for 30 min) also reduced the linear motion, but to a lesser extent (Fig. 4d, Supplementary Video 5 online). The decrease in the fraction of particles undergoing linear motion was statistically significant in both cases (Fig. 4e; t-test p-values $< 10^{-10}$). These results imply that the linear component of CD36 motion may depend on receptor engagement with both microtubules and cortical actomyosin. They also illustrate the ability of the tracker to distinguish random

motion from linear motion: Inclusion of an explicit linear motion model did not generate artificial linear tracks under drug perturbations.

Under all conditions, the CD36 receptors and receptor aggregates underwent merging and splitting events (Fig. 4f highlights two examples of merging and splitting particles, illustrating the strong geometric and intensity cues for merge and split events). We calculated the conditional probability of particles merging and splitting while undergoing linear motion vs. the conditional probability of merging and splitting while undergoing random motion (Fig. 4g) (Supplementary Note 11 online discusses the conditional probability analysis). For control as well as drug perturbation experiments, the conditional probability of merging and splitting while undergoing linear motion was about two times higher than the conditional probability while undergoing random motion. This implies that CD36 receptors moving along linear tracks aggregated and dissociated about twice as often as CD36 receptors not moving along linear tracks. Importantly, there were no significant differences between control and drug perturbation experiments in terms of the conditional probabilities and their ratios (p -values > 0.01). These findings indicate that the motion along linear tracks increases the association and dissociation of CD36 receptors, regardless of whether the receptors are in control or in drug-perturbed cells.

Discussion

This paper presents an algorithm for single particle tracking in complex live cell image sequences. The algorithm utilizes one compact mathematical framework, the linear assignment problem, to first link particles between consecutive frames, and then to close gaps and capture merging and splitting events between the initial track segments. In both steps, particle and track segment assignments are accomplished by spatially global optimization, increasing tracking accuracy under high-particle density conditions. In addition, track segment assignment in the second step is accomplished by temporally global optimization. The combination of these two optimization conditions brings our algorithm close to the theoretically best, yet practically too expensive, multiple-hypothesis tracking approach. While MHT generates tracks by constructing all possible paths starting from particle positions in all frames, our algorithm generates tracks by constructing in the second step all possible paths, starting from the initial track segments obtained in the first step. Starting with track segments substantially reduces the combinatorial space of potential assignments, bringing the solution of the assignment problem into the realm of high-end computing on a state-of-the-art desktop workstation. The price to pay for this reduction in computational complexity is that the initial track segments are generated in a greedy approach which can lead to irreparable particle assignment errors. However, this limitation can be circumvented by imposing conservative cutoffs on particle assignment in the first step, and then rescuing the resulting track interrupts in the second step, which – because of its temporal globality – is less prone to error and can afford wider cutoffs. Thus, by balancing the cutoffs of the first and second assignment steps, our method yields effectively an MHT solution.

The algorithm is highly versatile and applicable to a broad set of tracking tasks in live cell imaging. We have used this framework to track cell motility in tissue culture, chromosome

motion in 3D, synaptic vesicles, and cytoskeleton dynamics. Here, we showed two applications that highlight two of the most important features of our tracking algorithm. The endocytosis study critically depended on the algorithm's ability to produce complete tracks in dense particle fields, yielding reliable lifetime distributions for all CCPs in the field of view. The CD36 study critically depended on the algorithm's ability to capture merge and split events, and thus reveal the association and dissociation of receptors on a single molecule level. Both the CCP and the CD36 studies revealed the existence of mechanisms by which a cell might organize the kinetics and dynamics of signal transduction at the level of the plasma membrane. The power of a robust SPT algorithm, in combination with specific molecular interventions, will allow us to uncover the molecular mechanisms underlying this organization in the context of living cells.

Materials and Methods

Software

The tracking software is available for download at <http://lccb.scripps.edu>. Software details are provided in Supplementary Note 12 online.

CCP labeling and imaging

BSC1 (monkey kidney epithelial) cells stably expressing rat brain clathrin light chain-EGFP (kindly provided by T. Kirchhausen, Harvard Medical School, Boston, MA) were cultured and prepared as specified in Supplementary Note 13 online. For live cell imaging, BSC1 cells were plated on glass coverslips, and through-the-objective TIR-FM was performed on a Nikon TE2000U inverted microscope using a 100X/1.45NA oil-immersion objective. Images were captured at 0.5 Hz with 200ms exposure time using a Hamamatsu Orca II-ERG.

CD36 receptor labeling and imaging

Human primary macrophages were isolated from human blood samples and cultured in medium as specified in Supplementary Note 13 online. Immunolabeling of individual CD36 receptors was accomplished by incubation of cells first with anti-CD36 Fab fragments derived from mouse monoclonal antibodies to human CD36, and then with Cy3-conjugated donkey anti-mouse Fab fragments. Live-cell imaging was performed using a Zeiss Axiovert 200 inverted epifluorescence microscope equipped with a 100X/1.45NA oil-immersion objective. Image streams were captured at 10 Hz for 10 seconds using an EM-CCD camera (Hamamatsu).

Supplementary Material

Refer to Web version on PubMed Central for supplementary material.

Acknowledgements

This research was supported by the National Institutes of Health R01 grant GM73165 to GD and SLS, by grants from the Heart and Stroke Foundation of Canada and the Canadian Institutes for Health Research to SG, and by a postdoctoral fellowship from The Helen Hay Whitney Foundation/The Agouron Institute to KJ.

References

1. Sako Y, Minoguchi S, Yanagida T. Single-molecule imaging of EGFR signalling on the surface of living cells. *Nat Cell Biol.* 2000; 2:168–172. [PubMed: 10707088]
2. Fujiwara T, Ritchie K, Murakoshi H, Jacobson K, Kusumi A. Phospholipids undergo hop diffusion in compartmentalized cell membrane. *J Cell Biol.* 2002; 157:1071–1081. [PubMed: 12058021]
3. Groc L, et al. Differential activity-dependent regulation of the lateral mobilities of AMPA and NMDA receptors. *Nat Neurosci.* 2004; 7:695–696. [PubMed: 15208630]
4. Meijering E, Smal I, Danuser G. Tracking in molecular bioimaging. *IEEE Signal Proc Mag.* 2006; 23:46–53.
5. Kalaidzidis Y. Intracellular objects tracking. *Eur J Cell Biol.* 2007; 86:569–578. [PubMed: 17646017]
6. Ghosh RN, Webb WW. Automated Detection and Tracking of Individual and Clustered Cell-Surface Low-Density-Lipoprotein Receptor Molecules. *Biophys J.* 1994; 66:1301–1318. [PubMed: 8061186]
7. Crocker JC, Grier DG. Methods of Digital Video Microscopy for Colloidal Studies. *J Colloid Interf Sci.* 1996; 179:298–310.
8. Cheezum MK, Walker WF, Guilford WH. Quantitative Comparison of Algorithms for Tracking Single Fluorescent Particles. *Biophys J.* 2001; 81:2378–2388. [PubMed: 11566807]
9. Goulian M, Simon SM. Tracking single proteins within cells. *Biophys J.* 2000; 79:2188–2198. [PubMed: 11023923]
10. Schmidt T, Schutz GJ, Baumgartner W, Gruber HJ, Schindler H. Imaging of single molecule diffusion. *Proc Natl Acad Sci USA.* 1996; 93:2926–2929. [PubMed: 8610144]
11. Manley S, et al. High-density mapping of single-molecule trajectories with photoactivated localization microscopy. *Nat Methods.* 2008; 5:155–157. [PubMed: 18193054]
12. Reid DB. An algorithm for tracking multiple targets. *IEEE T Automat Contr.* 1979; 24:843–854.
13. Blackman, SS.; Popoli, R. Design and Analysis of Modern Tracking Systems. Norwood, MA: Artech House; 1999.
14. Veenman CJ, Reinders MJT, Backer E. Resolving Motion Correspondence for Densely Moving Points. *IEEE T Pattern Anal.* 2001; 23:54–72.
15. Chetverikov D, Verestoy J. Feature Point Tracking for Incomplete Trajectories. *Computing.* 1999; 62:321–338.
16. Shafique K, Shah MA. Noniterative Greedy Algorithm for Multiframe Point Correspondence. *IEEE T Pattern Anal.* 2005; 27:51–65.
17. Sbalzarini IF, Koumoutsakos P. Feature point tracking and trajectory analysis for video imaging in cell biology. *J Struct Biol.* 2005; 151:182–195. [PubMed: 16043363]
18. Genovesio A, et al. Multiple particle tracking in 3-D+t microscopy: Method and application to the tracking of endocytosed quantum dots. *IEEE T Image Process.* 2006; 15:1062–1070.
19. Tvarusko W, et al. Time-resolved analysis and visualization of dynamic processes in living cells. *Proc Natl Acad Sci USA.* 1999; 96:7950–7955. [PubMed: 10393928]
20. Jiang S, Zhou XB, Kirchhausen T, Wong STC. Tracking molecular particles in live cells using fuzzy rule-based system. *Cytom Part A.* 2007; 71A:576–584.
21. Bonneau S, Dahan M, Cohen LD. Single Quantum Dot Tracking Based on Perceptual Grouping Using Minimal Paths in a Spatiotemporal Volume. *IEEE T Image Process.* 2005; 14:1384–1395.
22. Genovesio A, Olivo-Marin J-C. Split and merge data association filter for dense multi-target tracking. *IEEE ICPR'04.* 2004; 4:677–680.
23. Racine V, et al. Visualization and quantification of vesicle trafficking on a three-dimensional cytoskeleton network in living cells. *J Microsc - Oxford.* 2007; 225:214–228.
24. Burkard, KE.; Cela, E. Handbook of Combinatorial Optimization -Supplement Volume A. Du, DZ.; Pardalos, PM., editors. Dordrecht, NL: Kluwer Academic Publishers; 1999. p. 75-149.
25. Jonker R, Volgenant A. A Shortest Augmenting Path Algorithm for Dense and Sparse Linear Assignment Problems. *Computing.* 1987; 38:325–340.

26. Ehrlich M, et al. Endocytosis by Random Initiation and Stabilization of Clathrin-Coated Pits. *Cell*. 2004; 118:591–605. [PubMed: 15339664]
27. Merrifield CJ, Feldman ME, Wan L, Almers W. Imaging actin and dynamin recruitment during invagination of single clathrin-coated pits. *Nat Cell Biol*. 2002; 4:691–698. [PubMed: 12198492]
28. Rappoport JZ, Simon SM. Real-time analysis of clathrin-mediated endocytosis during cell migration. *J Cell Sci*. 2003; 116:847–855. [PubMed: 12571282]
29. Merrifield CJ, Perais D, Zenisek D. Coupling between clathrin-coated-pit invagination, cortactin recruitment, and membrane scission observed in live cells. *Cell*. 2005; 121:593–606. [PubMed: 15907472]
30. Olivo-Marin J-C. Extraction of spots in biological images using multiscale products. *Pattern Recogn*. 2002; 35:1989–1996.
31. Conner SD, Schmid SL. Regulated portals of entry into the cell. *Nature*. 2003; 422:37–44. [PubMed: 12621426]
32. Macia E, et al. Dynasore, a cell-permeable inhibitor of dynamin. *Dev Cell*. 2006; 10:839–850. [PubMed: 16740485]
33. Febbraio M, Hajjar DP, Silverstein RL. CD36: a class B scavenger receptor involved in angiogenesis, atherosclerosis, inflammation, and lipid metabolism. *J Clin Invest*. 2001; 108:785–791. [PubMed: 11560944]
34. Thomann D, Rines DR, Sorger PK, Danuser G. Automatic fluorescent tag detection in 3D with super-resolution: application to the analysis of chromosome movement. *J Microsc - Oxford*. 2002; 208:49–64.

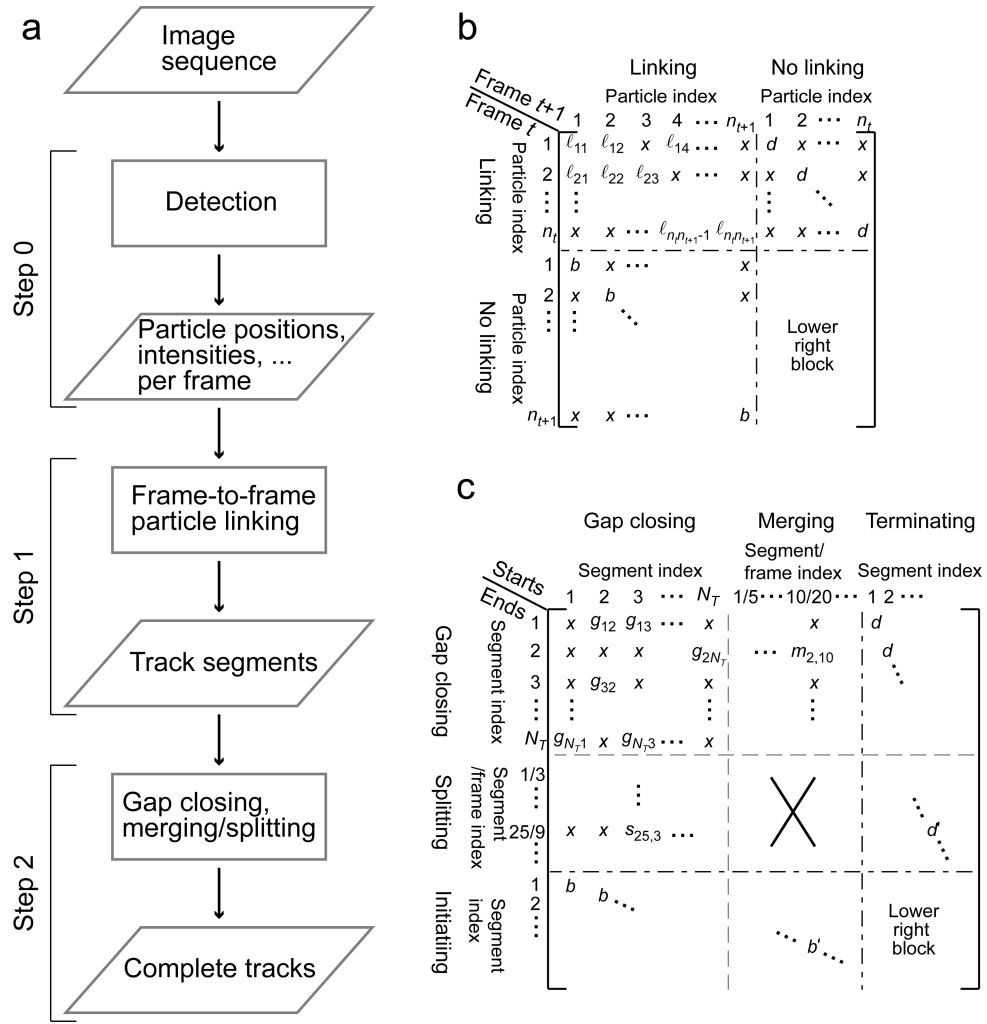


Figure 1. Tracking particles via spatially and temporally global assignments
(a) Tracks were constructed from an image sequence by detecting particles in each frame (Step 0), linking particles between consecutive frames (Step 1), and then closing gaps and capturing merging and splitting events between the initial track segments (Step 2). **(b)** Cost matrix controlling particle assignments between frames. λ_{ij} : cost for linking particle i in frame t to particle j in frame $t + 1$, x : impossible link whose cost exceeded the cutoff, d : cost for allowing particles in frame t to link to nothing in frame $t + 1$, b : cost for allowing particles in frame $t + 1$ to get linked by nothing in frame t . The lower right block is an auxiliary block required to satisfy the topological constraints of the LAP (Supplementary Note 4 online). **(c)** Cost matrix controlling gap closing, merging and splitting. g_{IJ} : cost for closing a gap between the end of track segment I and the start of track segment J , m_{IJ} : cost for the end of track segment I merging with a middle point of track segment J , s_{IJ} : cost for the start of track segment J splitting from a middle point of track segment I . Central cross: links between track segment middle points introduced for merging and splitting were not allowed. The upper and middle right blocks, lower left and middle blocks, and lower right block were as described in (b). In (b) and (c), ‘...’ means index continuation.

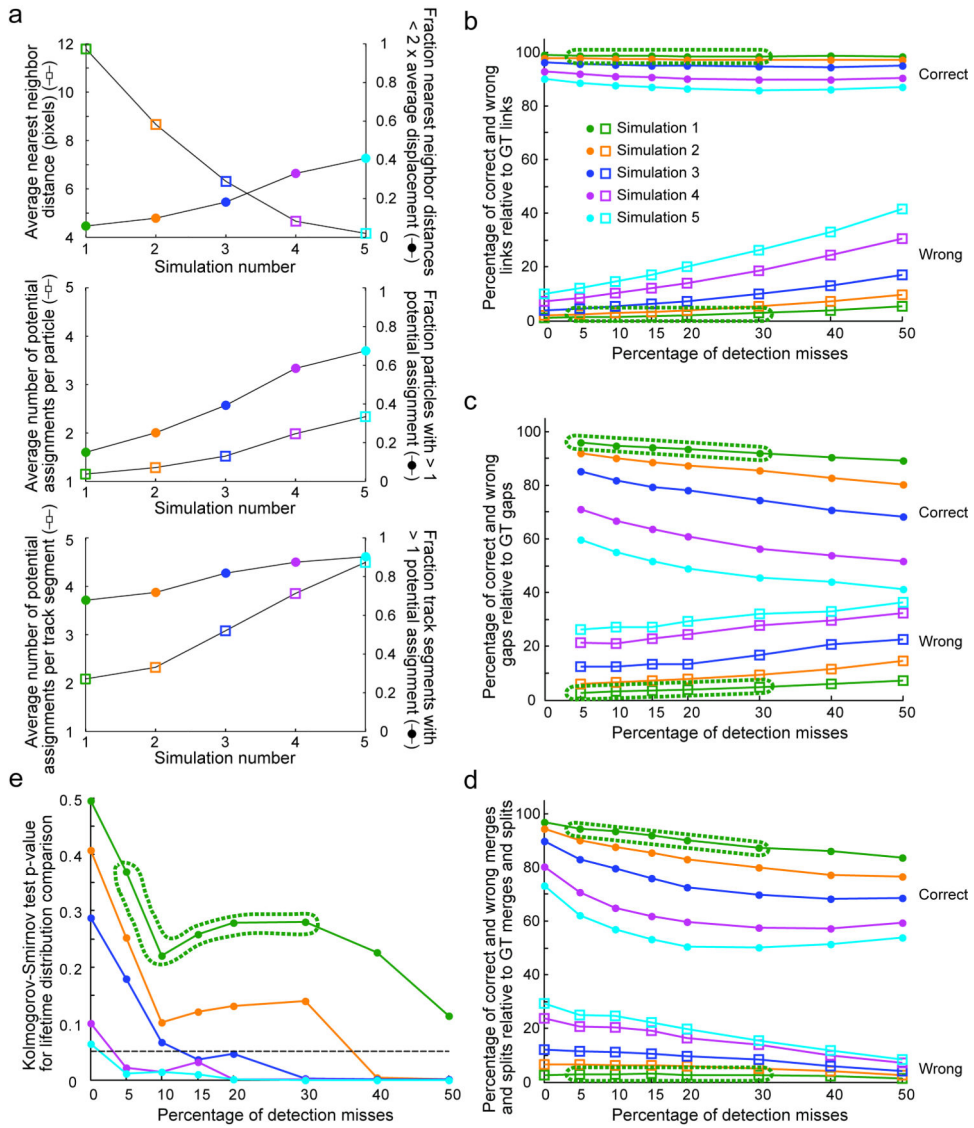


Figure 2. Validation of tracking algorithm on simulated tracks
 5 simulations of increasing particle density, each combined with 8 detection efficiencies represented by percentages of particles missing from the detection, were used to test the performance of the tracking algorithm. The results shown are the averages over 6 repetitions of each simulation. **(a)** Criteria to assess particle density as related to tracking: Average nearest neighbor distance (upper panel, left y-axis) and fraction of particles with nearest neighbors closer than twice their average frame-to-frame displacement (upper panel, right y-axis), evaluated at 0% detection misses; average number of potential assignments per particle (middle panel, left y-axis) and fraction of particles with > 1 potential assignment (middle panel, right y-axis) in the frame-to-frame linking step, evaluated at 0% detection misses; average number of potential assignments per track segment (lower panel, left y-axis) and fraction of track segments with > 1 potential assignment (lower panel, right y-axis) in the gap closing, merging and splitting step, evaluated at 20% detection misses (at 0% misses, there are no gaps to close). **(b–d)** Percentage of true and false positives in particle

linking (**b**), gap closing (**c**) and merging and splitting (**d**) relative to the ground truth (GT). (**e**) P-value of the Kolmogorov-Smirnov test comparing the measured and GT lifetime distributions. The 0.05 significance threshold is indicated by a dashed line. In (b–e), the conditions similar to the experimental data are highlighted with a dotted oval.

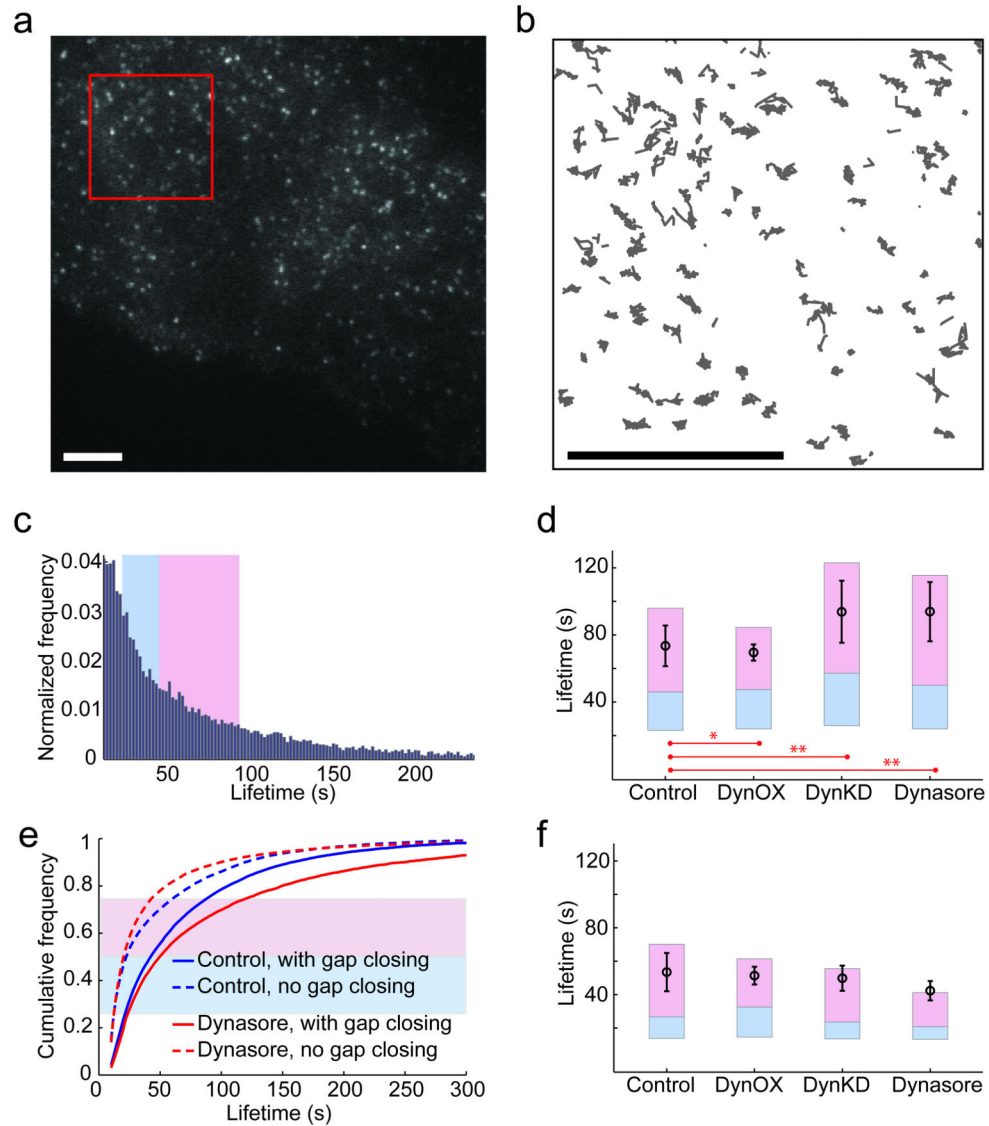


Figure 3. Clathrin-coated pit lifetime is regulated by dynamin

(a) TIR-FM image of a BSC1 cell fluorescently labeled with clathrin light chain-EGFP. Scale bar = 5 μm . (b) Clathrin-coated pit (CCP) trajectories in the $10 \times 10 \mu\text{m}$ area indicated by a red box in (a). (c) Normalized lifetime histogram of 21,518 CCP trajectories pooled from 11 control cell movies. Shaded blue and pink areas: second and third data quartiles. (d) CCP lifetimes for control and for alterations of dynamin function (DynOX: Dynamin over-expression, DynKD: Dynamin knockdown). Blue and pink bars: second and third data quartiles. Round black markers: mean. Black error bars: Cell-to-cell standard deviation (calculated for 11 control, 4 DynOX, 15 DynKD and 5 dynasore). KS-test: * p-value $< 10^{-5}$, ** p-value $< 10^{-10}$. (e) Cumulative frequency of CCP lifetimes in control and dynasore treated cells, resulting from tracking with gap closing (as in (b–d)) and without gap closing. (f) CCP lifetimes for control and for alterations of dynamin function resulting from tracking without gap closing.

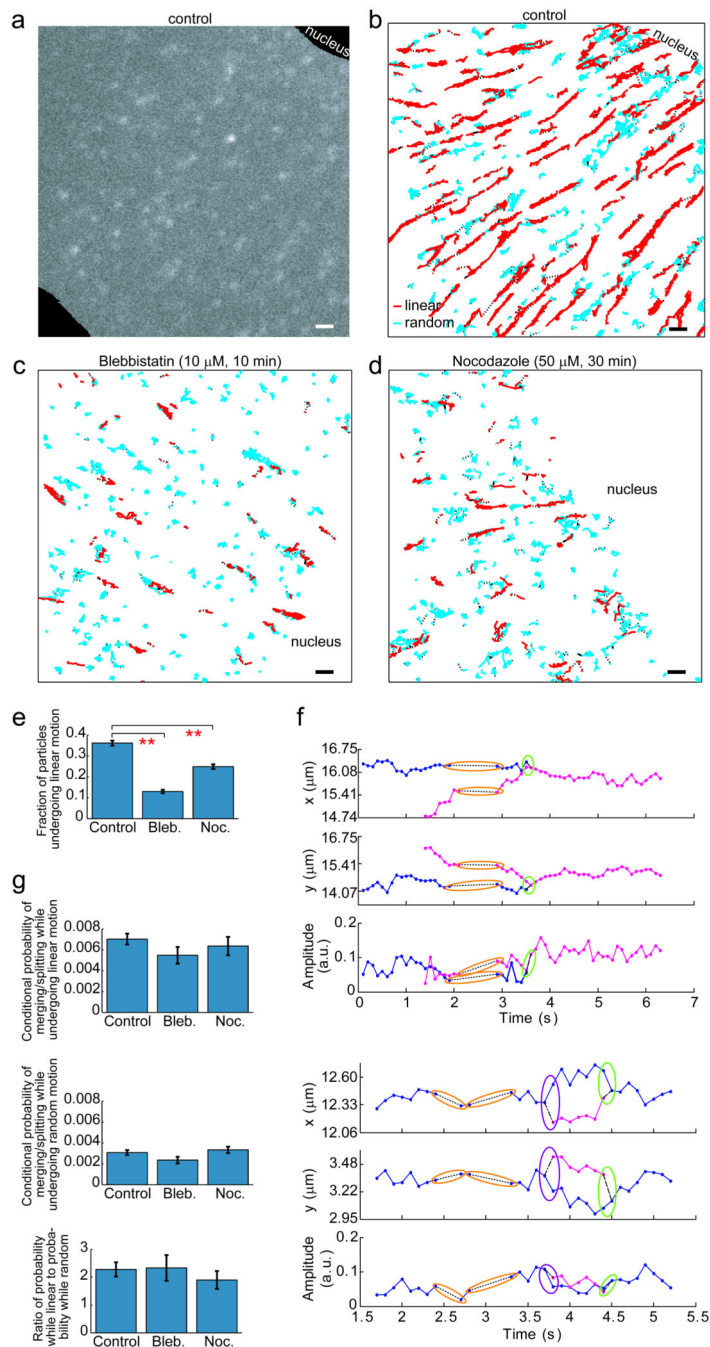


Figure 4. CD36 receptor aggregation activity depends on motion type
(a) Epifluorescence image of CD36 immuno-labeled in a control macrophage using a primary Fab fragment followed by a Cy3-conjugated secondary Fab fragment. **(b)** CD36 tracks in a control macrophage. **(c)** CD36 tracks in a Blebbistatin (Bleb.) treated macrophage. **(d)** CD36 tracks in a Nocodazole (Noc.) treated macrophage. All tracks are from 10s/100 frame movies. Tracks are classified as linear (red) or random (cyan) (Supplementary Note 10 online). Scale bar = 1 μm . **(e)** Fraction of particles undergoing linear motion. **(f)** Two sample trajectories represented as x-coordinate, y-coordinate and

amplitude over time, highlighting merging events (green ovals), splitting events (purple ovals) and closed gaps (orange ovals). The two colors (pink and blue) highlight the two track segments brought together by capturing merge and split events. **(g)** Conditional probabilities of merging and splitting while undergoing linear motion and while undergoing random motion, and ratio of conditional probability while undergoing linear motion to conditional probability while undergoing random motion. In **(e)** and **(g)**, error bars indicate standard deviation as calculated from a sample of size 200 generated by the bootstrap method. ** p-value $< 10^{-10}$. Statistics were calculated from 14 control cells (7527 trajectories ≥ 5 frames long), 11 Blebbistatin-treated cells (5148 trajectories ≥ 5 frames long) and 12 Nocodazole-treated cells (4926 trajectories ≥ 5 frames long). Trajectories shorter than 5 frames were excluded as non-classifiable with respect to motion type.